Journal of The Electrochemical Society, **156** (5) B580-B587 (2009)
0013-4651/2009/156(5)/B580/8/$23.00 © The Electrochemical Society

Growth, Characterization, and Electrochemical Properties of Doped n-Type $KTaO_3$ Photoanodes

I. E. Paulauskas,[a,z] J. E. Katz,[b] G. E. Jellison, Jr.,[c] N. S. Lewis,[b,*] L. A. Boatner,[c,d] and G. M. Brown[e,*]

[a]*Department of Materials Science and Engineering, The University of Tennessee, Knoxville, Tennessee 37996, USA*
[b]*Beckman Institute and Kavli Nanoscience Institute, Division of Chemistry and Chemical Engineering, California Institute of Technology, Pasadena, California 91125, USA*
[c]*Materials Science and Technology Division, and* [d]*Center for Radiation Detection Materials and Systems, and* [e]*Chemical Sciences Division, Oak Ridge National Laboratory, Oak Ridge, Tennessee 37831-6119, USA*

The effects of compositionally induced changes on the semiconducting properties, optical response, chemical stability, and overall performance of $KTaO_3$ photoanodes in photoelectrochemical (PEC) cells have been investigated. Single crystals of n-type Ca- and Ba-doped $KTaO_3$ with carrier concentrations ranging from 0.45 to 11.5 $\times$ 10^{19} cm^{-3} were grown and characterized as photoanodes in basic aqueous electrolyte PEC cells. The PEC properties of the crystals, including the photocurrent, photovoltage, and flatband potential in contact with 8.5 M NaOH(aq) were relatively independent of whether Ca or Ba was used to produce the semiconducting form of $KTaO_3$. All of the Ca- or Ba-doped $KTaO_3$ single-crystal photoanodes were chemically stable in the electrolyte and, based on the open-circuit potential and the band-edge positions, were capable of unassisted photochemical H_2 and O_2 evolution from H_2O. The minority-carrier diffusion lengths values were small and comparable to the depletion region width. Photoanodic currents were only observed for photoanode illumination with light above the bandgap (i.e., $\lambda < 340$ nm). The maximum external quantum yield occurred at $\lambda = 255$ nm (4.85 eV), and the depletion width plus the minority-carrier diffusion length ranged from 20 to 65 nm for the various $KTaO_3$-based photoanode materials.
 [DOI: 10.1149/1.3089281]

Manuscript submitted July 31, 2008; revised manuscript received January 21, 2009. Published March 10, 2009.

Photoelectrochemical (PEC) cells provide an energy-conversion mechanism through which light can be directly converted into a chemical fuel or electrical energy. PEC cells that are capable of evolving $H_2(g)$ from aqueous solutions are of particular interest because they offer a potential method for directly generating hydrogen fuel through the use of solar energy. However, no existing PEC system is presently capable of efficiently converting sunlight to hydrogen gas without an applied bias voltage.

In a typical PEC cell, electron-hole pairs are formed in the semiconductor on the absorption of photons having an energy greater than the bandgap of the material. These electron-hole pairs are separated by diffusion gradients or by the electric field present at the semiconductor-liquid interface (Fig. 1). If the photoanode is in contact with an alkaline electrolyte, the majority-carrier electrons are driven to the back contact and eventually reduce an acceptor species at a counter electrode to form hydrogen via the reaction

$$4H_2O + 4e^- \rightarrow 2H_2 + 4OH^- \quad [1]$$

The minority-carrier photogenerated holes flow in the opposite direction and oxidize the donor species at the semiconductor-liquid interface, producing oxygen through the reaction

$$4OH^- \rightarrow O_2 + 2H_2O + 4e^- \quad [2]$$

These equations combine to give the overall cell reaction

$$2H_2O \xrightarrow{h\nu} 2H_2 + O_2 \quad [3]$$

PEC cells can thus provide a method for the direct conversion of solar energy into hydrogen, producing a fuel that can be stored and transported for subsequent use.

Several fundamental requirements exist, however, in order for any PEC cell to be useful for converting solar energy into chemical fuel or electrical power. First, the photoelectrode must strongly absorb sunlight and efficiently produce electron-hole pairs. Second, these electron-hole pairs must be separated and collected. Finally, the charge carriers must be energetically and kinetically capable of driving the chemical reactions associated with water dissociation, while minimizing deleterious ancillary processes, such as the corrosion of the electrode itself. Appropriate values of the bandgap and of the absolute positions of the conduction and valence bands relative to the electrochemical potentials for H_2 and O_2 evolution in water are critical for efficient water dissociation based on PEC cells. The bandgap must be sufficiently small (optimally <2.0 eV) so that a significant portion of the Sun's energy is captured and converted, and additionally, the positions of the bottom of the conduction band, E_{CB}, and the top of the valence band, E_{VB}, must be above and below the positions of the hydrogen and oxygen evolution potentials, re-

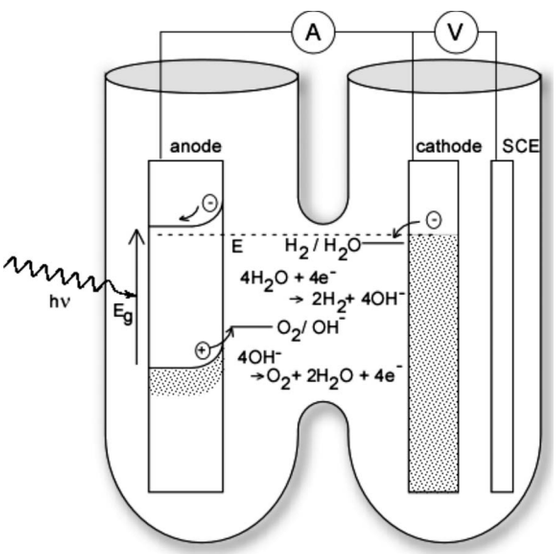

Figure 1. Schematic representation of a PEC cell using an n-type semiconducting photoanode in an alkaline electrolyte. When light strikes the anode, electron-hole pairs are formed and then separated by the electric field that is present due to the band bending at the surface of the semiconductor. Oxygen is formed at the surface of the semiconductor, while hydrogen is formed at the surface of the cathode, in this case, Pt.

* Electrochemical Society Active Member.
z E-mail: ipaulaus@utk.edu

spectively. These constraints impose a thermodynamic limit on the minimum bandgap of >1.23 eV for a single-photon threshold device.[1] Several semiconducting photoanodes, such as $SrTiO_3$,[2] ZrO_2, Ta_2O_5, and others,[3] split water efficiently with no applied bias voltage and are photochemically stable, but unfortunately, their large bandgaps (3.4–3.7 eV) prohibit significant absorption and conversion of most of the terrestrial solar spectrum.

The factors that control the stability of semiconductor photoanodes are among the least-well-understood aspects of PEC cells. The oxidation of water to O_2 is a four-electron process that proceeds through a series of partial reactions, generally creating highly reactive radical intermediates that are bound to the semiconductor surface. The intermediates must remain on the electrode surface to facilitate the subsequent oxidation steps in the electrolysis reaction, yet these intermediates may be capable of weakening or breaking bonds associated with the surface atoms of the electrode. The properties essential for good catalytic action can, therefore, also lead to undesired corrosion reactions. All of the presently known photoelectrodes that are both thermodynamically capable of water splitting and kinetically stable under illumination in aqueous solutions, in fact, do not absorb a significant portion of the solar spectrum. In contrast, known materials (such as CdTe or InP) that do absorb sunlight efficiently cannot sustain unassisted photochemically induced water-splitting in a stable fashion.[4]

At least two approaches have the potential to overcome the limited light absorption of stable, wide bandgap, semiconducting photoanodes. One approach uses dye sensitization to extend the optical response of nanocrystalline metal oxide photoelectrodes.[5-7] In these devices, the surface of a mesoporous, wide bandgap semiconductor, such as TiO_2, is coated with a monolayer of sensitizer molecules (generally a Ru-polypyridyl complex). Upon light absorption by the dye, the photogenerated electron is injected into the conduction band of the semiconductor, creating a photocurrent at photon energies significantly below the bandgap of the semiconducting metal oxide electrode itself. These systems are capable of absorption of >920 nm photons, with quantum yields approaching unity and solar energy conversion efficiencies reported in excess of 10%.[6] This approach, however, has not (to date) been applied successfully to the efficient generation of H_2 and O_2 from water because the systems only operate efficiently in nonaqueous solvents and with the I_3^-/I^- redox couple as the electron shuttle in the electrolyte.

A second approach is to develop a material that inherently meets the three criteria for efficient unassisted PEC solar energy–based water splitting. Rather than using molecular surface modification, the bulk composition of the material can be altered, as has been demonstrated in the case of a nickel-doped indium tantalum oxide photoanode, to extend the optical absorption of an otherwise wide-bandgap semiconductor.[8] At sufficiently high levels, "dopant" atoms can serve not only to provide charge carriers, but also to potentially alter the intrinsic nature of the material, thereby affecting its crystal and band structure, optical absorption, and electronic properties. Predicting such effects via calculations is not yet possible, and the scope of relevant experimental data is also limited.[9]

In the present work, we have employed single crystals of $KTaO_3$ as a model stable semiconducting photoanode system to investigate the effects of compositional variations on the electronic properties of this material and to elucidate its associated performance as a photoanode in a PEC cell. Pure $KTaO_3$ is a highly resistive ($\sim 10^{15}$ Ω cm), cubic perovskite crystal with a bandgap of ~ 3.64 eV.[10] When doped with alkaline-earth impurities such as calcium or barium, the resistivity of $KTaO_3$ can be decreased to ~ 0.05 Ω cm.[11] Although n-type $KTaO_3$ is known to be a stable material that is capable of unassisted PEC water splitting,[12-15] the overall solar energy conversion efficiencies of this system are low, due to the wide bandgap and poor absorption of the solar spectrum. In this work, n-type $KTaO_3$ single crystals have been degenerately doped with Ca or Ba ions with the goal of altering the band structure as a means of "sensitizing" the $KTaO_3$ response to lower energy irradiation while maintaining the established chemical stability of $KTaO_3$ photoanodes during the operation of a PEC cell.

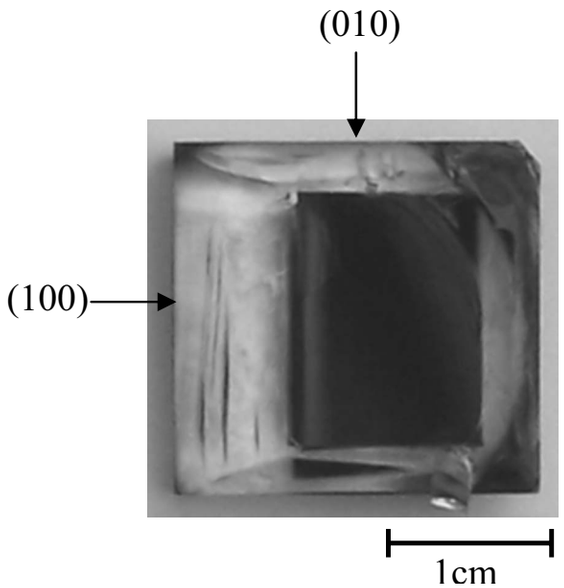

Figure 2. As-grown $KTaO_3$ single crystal. Crystals naturally grew with (100) faces (or equivalent faces), and two important regions could readily be distinguished visually: a dark central region, which is the n-type doped $KTaO_3$ ($\rho \sim 10^{-2}$ Ω cm) and a transparent region of pure and highly resistive $KTaO_3$ ($\rho \sim 10^{15}$ Ω cm).

The optical and electrochemical properties,[12-21] band structure,[10,22] and the crystal structure[23] of $KTaO_3$ have previously been studied in detail, both in the presence and absence of dopant atoms. This prior work, however, has not addressed how compositionally induced changes in semiconducting properties (such as the carrier concentration, mobility, and resistivity) affect the overall performance, optical response, and chemical stability of $KTaO_3$ photoelectrodes in operating PEC cells. Furthermore, the present work elucidates the positions of the band edges as a function of the dopant species and dopant concentration at the high dopant levels that are employed.

Experimental

Crystal growth and sample preparation.— The $KTaO_3$ single crystals used in the present studies were grown with a variety of dopant impurities by using the technique of solidification from a nonstoichiometric melt.[24] In this crystal-growth process, predetermined levels of the impurity were added to a Ta_2O_5 and K_2CO_3 mixture. Extra K_2CO_3 was also added to the growth charge to maintain an excess of K_2O that results from the thermal decomposition of potassium carbonate. The n-type semiconducting $KTaO_3$ single crystals were grown by adding the alkaline-earth elements Ca or Ba in their carbonate form ($CaCO_3$ or $BaCO_3$, respectively) to the $Ta_2O_5 + K_2CO_3$ mixture.

The crystal-growth charges were placed in Pt crucibles, covered with Pt sheets, and heated in air to 1390°C. The charges were then held at this temperature for 2 h, cooled at 1°C/h to 1350°C, at 0.75°C/h to 1300°C, and finally at 1°C/h to 900°C. At this point, the furnace was turned off but the crucibles remained in the furnace until room temperature was reached. The unreacted flux was then dissolved with water. The entire crystal growth process lasted ~21 days.

The crystals showed a well-defined rectangular or square cross section (Fig. 2). The dark central portion in Fig. 2 is the heavily doped region (resistivity, $\rho \sim 10^{-1}$ Ω cm), and the clear region is the undoped material ($\rho \sim 10^{15}$ Ω cm). This concentration gradient

in the dopant density is commonly reported for $KTaO_3$[20,25] and is a result of the effect of the segregation coefficient of impurities such as Ca and Ba.

The crystals naturally grew along their (100) faces, as determined by Laue X-ray back-reflection analysis. Photoanode samples were cut from the doped (dark) region of the crystal parallel to their longest (100) face to minimize the effects of dopant concentration gradients.[26] The specimens were then lapped and polished to form ~1 mm thick plates and were then finished with a 600-grit surface.

Immediately after polishing, ohmic contacts were made to the $KTaO_3$ plates by soldering a gold wire, using pure In dots, to a region of the crystal that had been coated with an In–Ga eutectic. The contacts were then covered with conducting silver paste. Insulating epoxy was used to cover the back contact surfaces and to define the surface area of the electrode that would be exposed to the electrolyte. Impedance spectra confirmed that the back contacts were ohmic. Exposed electrode areas were determined using Image SXM software by comparing a scanned image of the electrode surface to that of a template of known dimensions.

Companion Hall-effect samples were created on nominally square plates that had areas ranging from 21 to 70 mm^2. Ohmic contacts were made to these plates by coating indium on the four corners of the samples immediately after polishing. Hall-effect measurements were performed using the van der Pauw configuration.[27] The resistivities of the Ca- and Ba-doped samples were between 0.76×10^{-2} and 3.8×10^{-2} Ω cm, and the carrier concentrations varied from 0.4×10^{19} to 2×10^{19} cm^{-3}, consistent with prior reports of the properties of Ca-doped $KTaO_3$.[20] The carrier concentration varied by up to a factor of three within samples cut from the same crystal, presumably due to dopant segregation effects. The measured Hall mobilities ranged from 22 to 28.6 cm^2 V^{-1} s^{-1} and were somewhat lower than those reported previously,[11] possibly due to the presence of atomic-scale defects in the material.

Electrochemical methods.— The quartz electrochemical cell was H-shaped, with a porous frit separating the two cell compartments. One of the cell chambers had a flat quartz optical window (to transmit light longer than 180 nm) to facilitate UV illumination of the photoanode. Electrochemistry was performed in a 8.5 M NaOH(aq) (pH 14.9) solution at room temperature, with a Pt counter electrode and an aqueous saturated calomel reference electrode (SCE).

Electrochemical impedance spectroscopy.— Frequency-dependent impedance spectra were collected between 1 and 10^5 Hz using a Solartron model 1286 potentiostat and model 1260 impedance analyzer. The data were collected every 100 mV under reverse bias conditions for dc biases ranging from 0.9 to − 0.7 V vs SCE. The data were fit from 1 to 10^4 Hz to a three-element equivalent circuit that consisted of a resistor in series with a parallel combination of a capacitor and a resistor. The flatband potential, E_{FB}, and the carrier concentration, N_D, of the samples were determined by a conventional Mott–Schottky analysis of the impedance data using

$$\frac{1}{C_{SC}^2} = \frac{2}{q\varepsilon_0\varepsilon_S N_D A^2}\left(E - E_{FB} - \frac{kT}{q}\right) \qquad [4]$$

where C_{sc} is the space-charge capacitance (C cm^{-2}), E is the potential of the electrode (in volts), k is Boltzmann's constant, T is the temperature (in Kelvin), q is the charge on an electron, ε_0 is the dielectric constant of vacuum, ε_s is the static dielectric constant of $KTaO_3$,[11] and A is the electrode area (in centimeters squared). Extrapolation of C_{sc}^{-2} vs E to the x-intercept yielded $E_{FB} + kT/q$, and the slope yielded the dopant density of the sample. Details regarding this technique can be found elsewhere.[3,28] A least-squares linear analysis of the C_{sc}^{-2} vs E plots gave excellent fits to the data (Fig. 3). In certain cases, the data at large negative voltages were excluded, due to nonlinearity. Flatband potentials were found to be between −1.2 and −1.4 V vs SCE (Table I), which is comparable to the value reported by Bolts and Wrighton of −1.3 V vs SCE at pH 13 for n-type $KTaO_3$.[29]

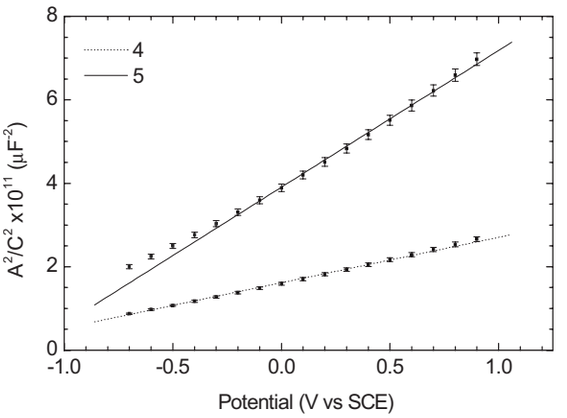

Figure 3. Mott–Schottky plots for Ca- (sample 4) and Ba- (sample 5) doped $KTaO_3$ crystals in a highly alkaline aqueous solution (details for $KTaO_3$ samples 4 and 5 can be found in Table I). At larger negative biases, as the bands are flattened, the differential capacitance of the space-charge region no longer dominates the total differential capacitance, and hence such data were excluded in the fits.

Current vs potential behavior.— Current density vs potential (J-E) data were obtained by illuminating the samples with a 150 W Xe arc lamp or an Oriel 66902 solar simulator with air mass (AM) 1.5 conditions. Data were collected at 50 mV s^{-1} in deoxygenated solutions, both in the dark and under illumination, using a Solartron model 1287 potentiostat. The J-E data obtained for all of the crystals showed rectification regardless of the type or concentration of the dopant (Fig. 4). Under simulated AM 1.5 illumination, the Ca- and Ba-doped $KTaO_3$ samples displayed mutual similar values of the current density at 0 V vs SCE (Table I).

To determine the open-circuit potential, E_{oc}, measurements were performed at constant photocurrent (50 μA at 0 V vs SCE). This facilitates the comparison of the E_{oc} values between samples under constant injection flux of minority carriers.[30] These measurements indicated that for the Ca- and Ba-doped samples, the E_{oc} values were similar (see Table I). The average E_{oc} between these samples was −1.36 V vs SCE with a standard deviation of ±0.1 V, which is in agreement with previous reports (E_{oc} = −1.25 V vs SCE).[14] In all cases, the E_{oc} values were more negative than the formal potential for the H^+/H_2 redox couple at the pH of concern [$E^{o\prime}(H^+/H_2)$ = −1.12 V vs SCE at pH 14.9].

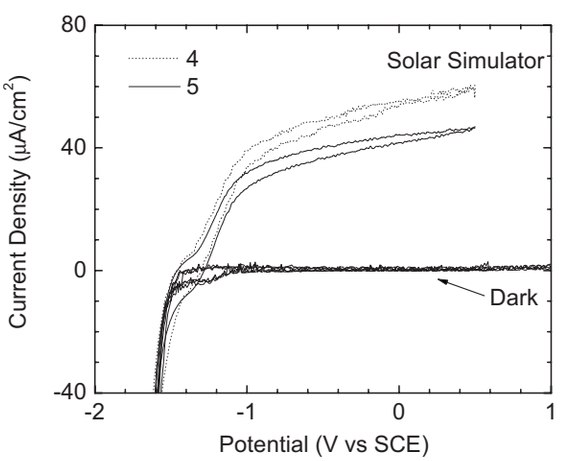

Figure 4. Photoresponse of selected $KTaO_3$ samples under AM 1.5 illumination. The current densities were low due to the small overlap with the solar spectrum.

Table I. Summary of photophysical properties for selected Ca- and Ba-doped $KTaO_3$ electrodes. The carrier concentrations and flatband potentials were determined using a Mott–Schottky analysis of the impedance spectra.

Sample	Dopant	Carrier concentration ($\times 10^{19}$ cm^{-3})	Flatband potential (V vs SCE)[a]	Conduction band potential (V vs SCE)[a]	Valence band potential (V vs SCE)	Maximum external quantum yield[b]	J under AM 1.5 illum. (μA/cm^2)[c]	E_{oc}[d] (V vs SCE)
1	Ca	0.46 ± 0.05	−1.24	−1.63	2.0 ± 0.3	0.30	42.7	−1.26
2		1.32 ± 0.19	−1.31	−1.67	1.9 ± 0.4	0.18	34.6	−1.34
3		4.70 ± 0.60	−1.21	−1.53	2.1 ± 0.4	0.15	19.7	−1.40
4		5.40 ± 0.50	−1.41	−1.73	1.9 ± 0	0.35	54.5	−1.47
5	Ba	0.40 ± 0.08	−1.16	−1.55	2.1 ± 0.3	0.21	44.5	−1.50
6		10.30 ± 2.10	−1.16	−1.46	2.1 ± 0.3	0.40	54.7	−1.28
7		11.50 ± 2.30	−1.28	−1.58	2.0 ± 0.1	0.29	52	−1.22

[a] Values ±0.02.
[b] Values ±0.01.
[c] Measured at 0 V vs SCE.
[d] Current density kept constant at 50 μA cm^{-2} by varying the light intensity.

Quantum yield.— Measurement of the quantum yield (Φ) included a determination of the quantum yield as a function of wavelength as well as a function of time for a given wavelength. The experimental setup consisted of a Xe arc lamp and a single-pass monochromator set at a 5 nm bandwidth. To reduce stray light in the monochromator resulting from the zeroth-order reflection from the grating, a BG-24 filter was placed at the entrance slit of the monochromator. The output beam was focused using a fused silica lens, and the intensity of the beam was continuously monitored by splitting off a portion of the light with a fused silica plate and directing the resulting split portion into a Si photodiode. A second National Institute of Standards and Technology (NIST)-calibrated Si diode was used to calibrate the illumination intensity incident on the sample. The photocurrent from the $KTaO_3$ electrodes at each wavelength was measured using a Princeton Applied Research model 2263 potentiostat/galvanostat.

Samples were held at 0 V vs SCE. Reflection losses due to the quartz window in contact with the electrolyte as well as the reflection from the electrode-electrolyte interface were taken into account. The illumination areas were ~1.7 mm^2 and were significantly smaller than the actual electrode surface.

Although all samples were measured using the dc method described, we also measured samples 2 and 5 (see Table I) using chopped light; no statistically significant difference between chopped data and the dc data was observed.

External quantum yield (Φ_{ext}) results indicate that the samples were photoactive at wavelengths <340 nm ($E > 3.64$ eV), with maximum external quantum yields ranging from 0.18 to 0.4 at 255 nm (Table I). Figure 5 shows the external quantum yield for various samples. The spectral response of all the samples exhibited a characteristic shape consisting of a broad peak (at 255 nm) followed by a tail between 300 and 340 nm. The observed behavior is consistent with the peak in the quantum yield reported previously by Ellis et al. at ~254 nm.[14] Additionally, Φ_{ext} was found to change within the same sample. Figure 6 shows two quantum yield data sets measured from sample 2; the only change in the measurements was the location of the illumination spot. Significant changes in Φ_{ext} only were observed at the lower wavelengths, with the maximum difference observed at the peak of the spectral response.

Time-resolved quantum yield measurements were performed at 260 and 320 nm. At both wavelengths, the decrease in Φ_{ext} from its initial value could be fit using a double exponential

$$\Phi_{ext}(\lambda) = A_0 + A_1 e^{-t/t_1} + A_2 e^{-t/t_2} \quad [5]$$

Results for a selected Ca- and a Ba-doped crystal are displayed in Table II. The data for sample 2 at 260 nm has been previously reported in Ref. 31, and is used in Table II for comparison purposes. The time constants indicate for both samples that Φ_{ext} reached equilibrium considerably faster at 320 nm (which is inside the tail region

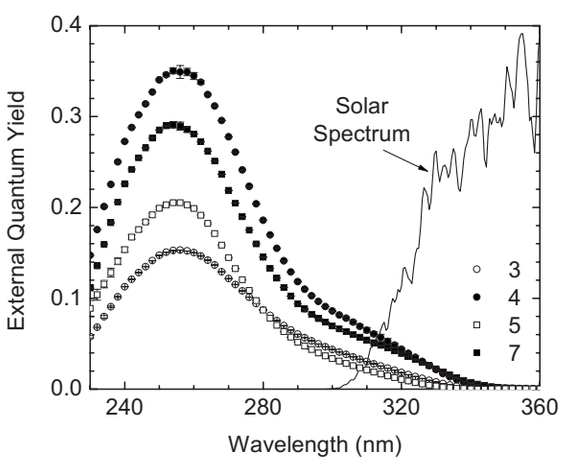

Figure 5. Spectral response for various Ca- (circles) and Ba- (squares) doped $KTaO_3$ samples. The AM 1.5 solar spectrum is also shown (in arbitrary units).

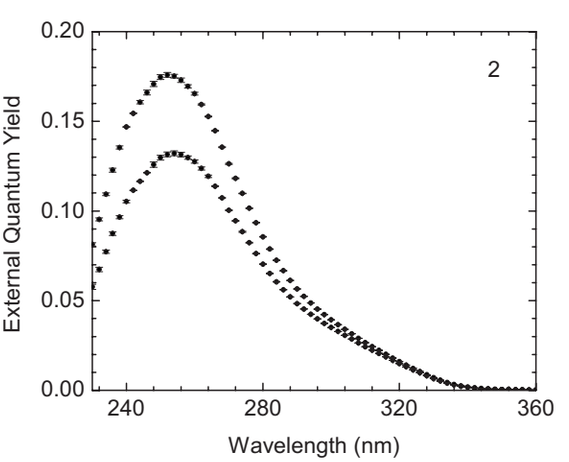

Figure 6. Variations of the external quantum yield for sample 2. Note that significant variations in the quantum yield were only observed at shorter wavelengths.

Table II. Exponential decay fitting parameters for the time-resolved quantum yield measurements.

Sample	Wavelength (nm)	Penetration Depth[a] (nm)	A_0[b]	A_1[c]	t_1 (s)	A_2[c]	t_2 (s)	χ^2[d]
2	260[e]	16	0.173	0.013	240 ± 20	0.009	3400 ± 30	0.72
	320	1100	0.017	0.002	18 ± 1	0.0007	160 ± 4	0.27
5	260	16	0.197	0.006	798 ± 95	0.006	5220 ± 300	0.07
	320	1100	0.015	0.001	8±1	—	—	1.35

[a] From Reference 10.
[b] Errors limits <1%.
[c] Error limits <7%.
[d] The reduced χ^2 is used as the figure of merit of the fit, where $\chi 2 \leq 1$ indicates a good fit.
[e] From Reference 31.

of the Φ_{ext} curve, see Fig. 5) than at 260 nm (the peak region). Some difficulties were present while measuring sample 5 at 320 nm, since the Φ_{ext} decay time constant approached 10 s, which is close to the time resolution of the system.

Additional time-resolved quantum yield measurements at 260 nm using a deoxygenated 8.5 M NaOH electrolyte at room temperature were performed to better analyze the possibility of oxygen formation at the surface of the $KTaO_3$ electrode as a function of time. Deoxygenation was achieved by sparging ultrahigh-purity He in the electrolyte. This process was initiated 1.5 h before the measurement started and was maintained throughout the measurement. The He sparging not only helped to keep the electrolyte deoxygenated but also reduced any mass transfer effects at the photoanode/electrolyte interface. The decreased photocurrent measured at the $KTaO_3$ electrode was also fit to a double exponential similar to Eq. 5, where $A_0 = 2$, $A_1 = 0.08$, $t_1 = 370 \pm 4$, $A_2 = 0.11$, and $t_2 = 5310 \pm 20$ ($R^2 = 0.90$).

Results and Discussion

J-E behavior of doped $KTaO_3$.— The observed low photocurrent densities were primarily the result of the small overlap of the $KTaO_3$ optical absorption range with the lamp's irradiance spectrum (Fig. 4 and 5), which has only a small fraction of its total power at wavelengths <300 nm. *J-E* data under illumination showed an inflection point at −1.4 V vs SCE. This behavior is commonly observed with metal oxide semiconductors. At more positive voltages, the band edges are sufficiently bent to efficiently collect photogenerated carriers. As the potential is scanned into the negative region, the bands are flattened, reducing the collection efficiency of photogenerated charge carriers to zero. However, due to the slow interfacial kinetics and deoxygenated electrolytes, essentially no dark current passes at these potentials, resulting in net zero current. Finally, as the applied potential is made sufficiently negative to overcome the overpotential for the reduction of water, a cathodic current is observed. The hysteresis observed in Fig. 4 between the reverse and forward scan direction was a function of the scan rate used (50 mV s^{-1}), indicating the presence of a time dependence in the measurements.

Mott–Schottky analysis.— Mott–Schottky analysis of the impedance spectra provided the values of the flatband potentials of the samples in the dark. Despite the consistency of the measured flatband potentials, values of N_D varied significantly among the samples, having values in the range of 0.4×10^{19}–12×10^{19} cm^{-3}. Self-segregation of dopants during the crystal growth process precluded extremely precise control of the doping levels.

Given the flatband potential and the dopant density, the potential of the bottom of the conduction band edge is given by

$$E_{CB} = E_{FB} - \frac{kT}{q} \ln\left(\frac{N_C}{N_D}\right) \quad [6]$$

where N_C is the effective density of states in the conduction band. Note that the second term in Eq. 6 is relatively small due to the large values of N_D. The value of N_C is

$$N_C = 2\left(\frac{2\pi m_e^* kT}{h^2}\right)^{3/2} = 1.42 \times 10^{19}\ \text{cm}^{-3} \quad \text{at} \quad 298\ \text{K} \quad [7]$$

where m_e^* is the effective mass of electrons in the conduction band[17] and h is Planck's constant.

Given the conduction-band edge and the bandgap, the position of the top of the valence band can be readily calculated. The position of the band edges was similar for the various samples (Table I), and in all cases, the H_2O/H_2 and O_2/OH^- formal potentials (−1.12 and 0.11 V vs SCE, respectively, at pH 14.9) fell within the bandgap of the $KTaO_3$, indicating that the samples are thermodynamically capable of electrolyzing water with zero applied bias.

As the electrode potential approaches the flatband potential, the depletion width goes to zero and the differential capacitance of the space-charge region increases so that the depletion region capacitance no longer dominates the total capacitance of the system. Other capacitive elements, such as that of the double layer, which, in the equivalent circuit, are in series with the space-charge region capacitance, will contribute significantly to the measured capacitance under such conditions. This was commonly observed as a deviation from linearity of the C_{sc}^{-2} vs E plots at potentials negative of −0.2 V vs SCE (Fig. 3). The data at potentials approaching flatband were thus excluded from the Mott–Schottky analysis.

Quantum yield.— The various samples all exhibited photocurrents over similar ranges of excitation energies, indicating that the replacement of K^+ with varying amounts of the electron donors Ca^{2+} and Ba^{2+} did not measurably sensitize the $KTaO_3$ to longer wavelengths illumination. This insensitivity to doping at these levels may be due to the dopant atoms, despite their high concentration, not forming a significant density of states within the bandgap. Alternatively, the newly formed states may lack a sufficiently strong interaction with the band states of intrinsic $KTaO_3$ to absorb visible light.

Optical measurements and quantum yields.— Spectroscopic ellipsometry and optical transmission data of both doped and undoped $KTaO_3$ indicate that the lowest optical gap in $KTaO_3$ is indirect, with an energy of 3.64 eV.[10] Three higher energy direct gaps also exist, with energies of 4.35, 4.68, and 5.03 eV, respectively. The data presented in Ref. 10 have been replotted in Fig. 7 to emphasize the characteristics of the optical absorption that are important in understanding the photoelectrochemistry of $KTaO_3$. Figure 7a depicts the penetration depth of light vs wavelength, where the

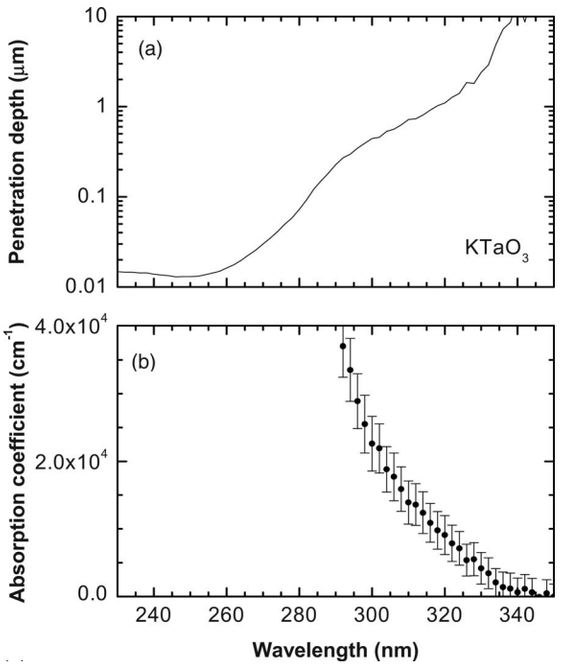

Figure 7. The penetration depth of light: (a) taken as the inverse of the absorption coefficient, from Ref. 10. (b) The absorption coefficient (including data from Ref. 10), is plotted to emphasize the linearity in the indirect bandgap region.

penetration depth is the inverse of the absorption coefficient, representing the depth at which the light intensity is reduced to $1/e$ ~37% of its incident value. As can be seen from this plot, light in the 300–340 nm region is preferentially absorbed ~1 μm from the surface of the sample.

One consequence of the deeper penetration of light is that the electron-hole pairs are generated far into the crystal and must diffuse to the depletion region near the surface to be collected. This constraint considerably reduces the quantum efficiency for photons generated at long wavelengths. Using the simple solar cell model,[32] it can be shown that for crystals exhibiting ideal behavior, the external quantum yield $[\Phi_{ext}(\lambda)]$ is described by

$$\Phi_{ext}(\lambda) = \frac{\alpha(\lambda)L}{\alpha(\lambda)L + 1}[1 - R(\lambda)] \quad [8]$$

where $\alpha(\lambda)$ is the optical absorption coefficient of the material, L is the minority-carrier diffusion length, and $R(\lambda)$ is the surface reflectance. In deriving Eq. 8, three important assumptions are made, as follows:

1. The depletion width (W) is considerably smaller than the penetration depth of light.
2. The cell thickness is large compared to L.
3. L is much larger than W.

Part of the usefulness of Eq. 8 is that it represents a simple way to utilize the experimentally measured values of Φ_{ext} to estimate the minority carrier diffusion length for semiconductors, such as single-crystal Si.[33] However, in cases where semiconductors exhibit a more complex, nonideal behavior, such as the degenerate n-type $KTaO_3$ used in this study, assumptions like those made in deriving Eq. 8 are no longer reasonable, and parameters like W become more important in understanding the PEC behavior of these crystals. If we assume that the cell thickness is considerably larger than L and W is much smaller than the penetration depth of light, then the internal quantum yield due to the base of the cell, $\Phi_{int,B}$, is given by

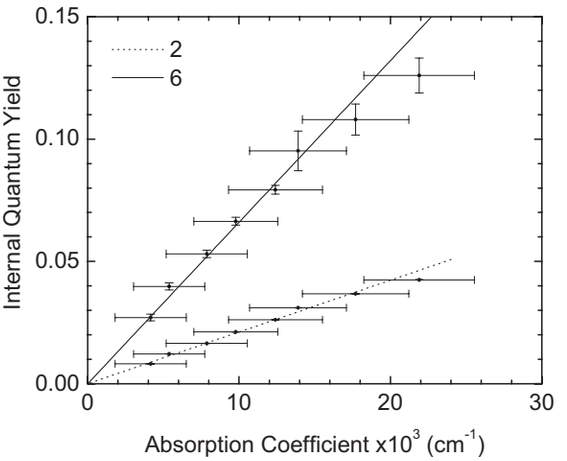

Figure 8. Internal quantum yields as a function of the absorption coefficient for representative Ca- (sample 2) and Ba- (sample 6) doped $KTaO_3$ crystals. Fitting of the data was performed by weighting the errors.

$$\Phi_{int,B}(\lambda) = \frac{\alpha(\lambda)L}{\alpha(\lambda)L + 1}\exp[-\alpha(\lambda)W] \quad [9]$$

Similarly, the internal quantum yield due to the depletion region, $\Phi_{int,DR}$, is given by

$$\Phi_{int,DR}(\lambda) = 1 - \exp[-\alpha(\lambda)W] \quad [10]$$

The total external quantum yield of the system is given by

$$\Phi_{ext}(\lambda) = [\Phi_{int,B}(\lambda) + \Phi_{int,DR}(\lambda)][1 - R(\lambda)] \quad [11]$$

Using Eq. 9 and 10, the external quantum yield of the system can be expressed as

$$\Phi_{ext}(\lambda) \approx \left\{1 - \frac{\exp[-\alpha(\lambda)W]}{\alpha(\lambda)L + 1}\right\}[1 - R(\lambda)] \quad [12]$$

where the quantum yield is not only linked to the minority carrier diffusion length, but also to the depletion width. Equation 12, and the absorption coefficient of $KTaO_3$ shown in Fig. 7b, imply that $\Phi_{ext}(\lambda)$ should decrease monotonically from ~300 to 340 nm, in accordance with observations (see Fig. 5 and 6).

Because Eq. 12 is less restrictive than Eq. 8 and still models an ideal system, it is a good starting point for understanding the PEC behavior of these degenerately doped semiconductors. Expanding Eq. 12 in a Taylor series and keeping only first-order terms yields

$$\Phi_{ext}(\lambda) \approx (W + L)\alpha(\lambda)[1 - R(\lambda)] \quad [13]$$

Equation 13 thus provides an expression that links W and L in a single term. Figure 8 shows a plot of Φ_{int} vs $\alpha(\lambda)$ for two representative samples, which according to Eq. 13, should result in a linear dependence with a slope proportional to $W + L$. For all fits, the multiple-correlation coefficient was 0.99.

To obtain approximate values for W, an ideal one-sided abrupt junction was assumed, and was estimated using[34]

$$W = \sqrt{\frac{2\varepsilon_s}{qN_D}\left(V_{bi} - \frac{2kT}{q}\right)} \quad [14]$$

where V_{bi} is the built-in voltage. Figure 9 shows the depletion-layer width (W) as a function of the carrier concentration, for three different values of V_{bi}. For our n-type $KTaO_3$ samples, W was estimated to range from 20 nm for the crystals with higher carrier concentrations ($\sim 10^{20}$ cm^{-3}) to 90 nm for the lower-doped crystals ($\sim 4 \times 10^{18}$ cm^{-3}).

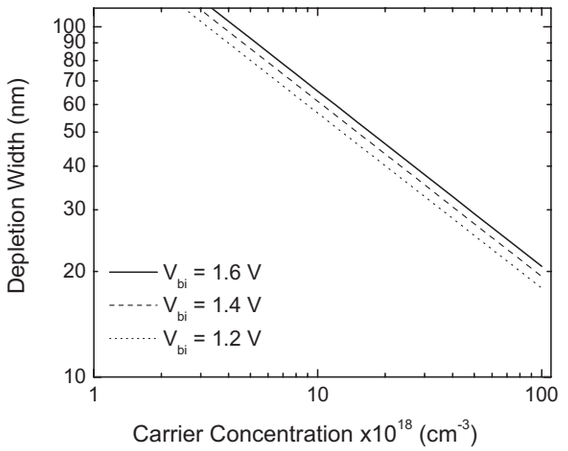

Figure 9. Estimated values of the depletion width, *W*, for the heavily doped $KTaO_3$ crystals as a function of the carrier concentration at the semiconductor/electrolyte interface. A one-sided "abrupt" junction is assumed.

Figure 10 shows the calculated slopes (from Eq. 13), expressed in nanometers, as a function of the carrier concentration for the Ca- and Ba-doped samples. Two points are immediately evident from this plot: (*i*) no obvious correlation is present between the slope and the carrier concentration and (*ii*) the slopes (ideally representing $W + L$) have comparable magnitudes to the estimated depletion width. This suggests that *L* and *W* have similar values and consequently are difficult to quantify individually or that additional issues (such as an inhomogeneous surface) make this system more complicated than the ideal case. As a result, the slope may represent all these effects taken together.

The noted differences in the quantum-yield behavior can be at least partially explained by the time-resolved data (Table II). As previously noted in Ref. 31, the observation of at least two time constants to define the decay behavior indicates that multiple electrically active defects reduce the quantum yield of the devices. The present study found that this double-exponential decay scheme was independent of the wavelength used or the doping species at these high carrier concentrations. Additionally, the magnitudes of the time constants indicate that when electron-hole pairs are formed near the surface of the crystal ($\lambda = 260$ nm has a penetration depth of

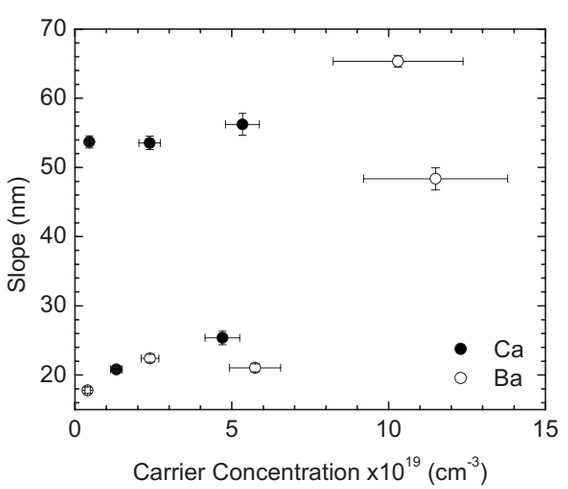

Figure 10. "Slope" of Eq. 13 (ideally representing the minority carrier diffusion length + the depletion width) vs the carrier concentration.

~16 nm), the time needed for the charge-collection process to reach equilibrium is much larger than when the electron-hole pairs are primarily formed deeper in the crystal ($\lambda = 320$ nm has a penetration depth of ~1100 nm) and away from the depletion region. Additionally, the relative decay of the quantum yield for a given sample was independent of wavelength. For sample 2, at 260 nm the percentage of reduction from the initial external quantum yield (A_0) to its equilibrium value ($A_1 + A_2$) was 12.7 ± 1.1%, while at 320 nm this reduction was 14.4 ± 0.5%. Similarly, the quantum yield decline changes for sample 5 at 260 and 320 nm were 6.1 ± 0.4% and 8.4 ± 0.6%, respectively.

Because of the large magnitude of the time constants obtained when light was preferentially absorbed at the surface of the electrodes, an additional time-resolved quantum yield curve was measured using a deoxygenated electrolyte in order to estimate the formation rate of O_2 molecules at the surface of the photoanode. The photoinduced current measured from the photoanode as a function of time has been fitted to a double exponential. This curve allowed the calculation of the total charge in coulombs used by the system, which can then determine the total amount of moles of electrons used per second. Using Eq. 1-3 to calculate the amount of moles of O_2 produced as a function of time, enables the rate of formation of O_2 molecules (assuming an O_2 molecule diameter of 0.29 nm) to be estimated. Knowing that the light spot size is 1.7 mm, in ideal circumstances it can be estimated that ~15% of the spot size could be covered by an O_2 monolayer after 1 s of illumination, if every electron measured is part of the water dissociation reaction.

These results suggest that at least two processes could be causing the reduction of quantum yield as a function of time. There is the possible formation of an oxygen monolayer that could effectively reduce the area for light absorption on the photoanode, which consequently will reduce the quantum yield; however, this process should equilibrate relatively rapidly since the entire light-spot area should be covered in ~7 s, and no bubbles were observed to form by optical examination of the cell during these measurements. The defects in the material may be susceptible to light-induced changes, whereby the light changes the defect into a recombination center. Obviously, there is a significant dependence on the penetration depth of light, where the light-induced change near the surface is considerably slower than the light-induced change further into the bulk of the material. Furthermore, there are significant sample-to-sample differences, particularly in the concentration of defects that are susceptible to light-induced changes. Another complication is that the quantum yield was never close to 1 for any of the samples studied. As a result, many of the electron-hole pairs created are lost to recombination centers, even for electron-hole pairs collected in the depletion region (for $\lambda = 260$ nm). This may mean that surface recombination plays an important role in determining the ultimate collection efficiency for $KTaO_3$ PEC cells. Clearly, a number of unanswered questions remain regarding the minority-carrier transport and recombination processes in these materials.

Conclusions

The addition of Ca^{2+} or Ba^{2+} (through the use of $CaCO_3$ and $BaCO_3$, respectively, in the crystal growth process) yielded highly doped n-type $KTaO_3$. The conductivities and carrier concentrations of these $KTaO_3$ samples were greatly increased as a result of doping and the doped crystals were dark blue.

The quantum yield of the n-type $KTaO_3$ photoanodes did not correlate with the alkaline-earth element (i.e., Ba vs Ca) used for doping. A photoresponse was only observed under UV irradiation ($\lambda \leq 340$ nm), reaching a maximum response at ~255 nm. Because <2% of the total radiance from the sun is <360 nm, additions of Ca or Ba did not offer an effective practical mechanism for improving the solar response of semiconducting $KTaO_3$. All of the heavily doped $KTaO_3$ photoanodes were found to be chemically

stable and, based on these open-circuit potentials and band-edge positions, were thermodynamically capable of unassisted photochemical H_2 and O_2 evolution from H_2O.

Determinations of the minority-carrier diffusion lengths suggest that these values are small and similar to those of the depletion-region width. Both factors will significantly increase the probability for the minority carriers to recombine, consistent with the observed reduction in quantum yield as the light was preferentially absorbed deeper in the crystal.

Time-resolved measurements indicated that, regardless of the penetration depth of the light, the quantum yield decrease was characterized by the presence of at least two time constants, which were associated with at least two types of electrically active defects. Although the reduction of the quantum yield may, in part, be associated with the formation of an oxygen layer at the surface of the semiconductor, it is also possible that the effect of the complex defects present in the semiconductor became significant when electron-hole pairs were formed near the surface of the semiconductor.

Ongoing experimental efforts are focused on finding more effective dopant species (or combinations thereof), exploring the possibility of significantly lowering the doping concentrations to increase the depletion region width as well as the minority carrier diffusion length, and the use of thermochemical reduction treatments as a means of sensitizing $KTaO_3$ to achieve more efficient PEC production of H_2 under terrestrial solar irradiation.

Acknowledgments

This research was sponsored by the Division of Materials Science and Engineering, Office of Basic Energy Sciences, U.S. Department of Energy, under contract no. DE-AC05-00OR22725 with Oak Ridge National Laboratory, managed and operated by UT-Battelle, LLC, and by the Office of Basic Energy Sciences, under grant no. DE-FG0Z-03ERI5483 with the California Institute of Technology. The authors acknowledge, with thanks, the contributions of J. O. Ramey, J. A. Kolopus, and H. E. Harmon to various aspects of this work.

University of Tennesse assisted in meeting the publication costs of this article.

References

1. A. J. Bard, R. Parsons, and J. Jordan, Editors, *Standard Potentials in Aqueous Solutions*, p. 54, Marcel Dekker, New York (1985).
2. M. S. Wrighton, A. B. Ellis, P. T. Wolczanski, D. L. Morse, H. B. Abrahamson, and D. S. Ginley, *J. Am. Chem. Soc.*, **98**, 2774 (1976).
3. A. J. Nozik, *Annu. Rev. Phys. Chem.*, **29**, 189 (1978).
4. N. S. Lewis, *Nature (London)*, **414**, 589 (2001).
5. M. Gratzel, *Inorg. Chem.*, **44**, 6841 (2005).
6. M. Gratzel, *J. Photochem. Photobiol. C*, **4**, 145 (2003).
7. M. Gratzel, *Nature (London)*, **414**, 338 (2001).
8. Z. G. Zou, J. H. Ye, K. Sayama, and H. Arakawa, *Nature (London)*, **414**, 625 (2001).
9. M. Woodhouse, G. S. Herman, and B. A. Parkinson, *Chem. Mater.*, **17**, 4318 (2005).
10. G. E. Jellison Jr., I. E. Paulauskas, L. A. Boatner, and D. J. Singh, *Phys. Rev. B*, **74**, 155130 (2006).
11. S. H. Wemple, *Phys. Rev.*, **137**, 1575 (1965).
12. L. A. Boatner, M. Linvill, and F. A. Modine, *Bull. Am. Phys. Soc.*, **24**, 274 (1979).
13. M. S. Wrighton, P. T. Wolczanski, and A. B. Ellis, *J. Solid State Chem.*, **22**, 17 (1977).
14. A. B. Ellis, S. W. Kaiser, and M. S. Wrighton, *J. Phys. Chem.*, **80**, 1325 (1976).
15. P. J. Boddy, D. Kahng, and Y. S. Chen, *Electrochim. Acta*, **13**, 1311 (1968).
16. P. E. Petersen, *J. Appl. Phys.*, **44**, 1240 (1973).
17. Z. Sroubek, *Phys. Rev. B*, **2**, 3170 (1970).
18. W. S. Baer, *J. Phys. Chem. Solids*, **28**, 677 (1967).
19. W. S. Baer, *Phys. Rev. Lett.*, **16**, 729 (1966).
20. L. S. Senhouse, M. V. Depaolis, and T. C. Loomis, *Appl. Phys. Lett.*, **8**, 173 (1966).
21. M. D. Agrawal and K. V. Rao, *J. Phys. C*, **3**, 1120 (1970).
22. A. Frova and P. J. Boddy, *Phys. Rev.*, **153**, 606 (1967).
23. K. Leung, *Phys. Rev. B*, **63**, 134415 (2001).
24. D. M. Hannon, *Phys. Rev.*, **164**, 164 (1967).
25. S. Aravazhi, A. Tapponnier, D. Gunther, and P. Gunter, *J. Cryst. Growth*, **282**, 66 (2005).
26. D. Rytz and H. J. Scheel, *J. Cryst. Growth*, **59**, 468 (1982).
27. L. J. Van der Pauw, *Philips Res. Rep.*, **13**, 1 (1958).
28. S. R. Morrison, *Electrochemistry at Semiconductor and Oxidized Metal Electrodes*, p. 127, Plenum Press, New York (1980).
29. J. M. Bolts and M. S. Wrighton, *J. Phys. Chem.*, **80**, 2641 (1976).
30. M. X. Tan, P. E. Laibinis, S. T. Nguyen, J. M. Kesselman, C. E. Stanton, and N. S. Lewis, *Progr. Inorg. Chem.*, K. D. Karlin, Editor, Vol. 41, p. 21, John Wiley & Sons, Inc., Hoboken, NJ (1994).
31. I. E. Paulauskas, J. E. Katz, G. E. Jellison Jr., N. S. Lewis, and L. A. Boatner, *Thin Solid Films*, **516**, 8175 (2008).
32. H. J. Hovel, *Semiconductors and Semimetals*, R. K. Willarnson and A. C. Beer, Editors, Vol. II, Academic Press, New York (1975).
33. M. L. Rosenbluth and N. S. Lewis, *J. Am. Chem. Soc.*, **108**, 4689 (1986).
34. S. M. Sze, *Physics of Semiconductor Devices*, 2nd ed., John Wiley & Sons, Hoboken, NJ (1981).